energies

MDPI

Article

Full-Speed Range Control Method of 390 kW Induction Motors in Railway System Using a HANPC Inverter

Do-Hyeon Kim, Min-Seong Kim and June-Seok Lee *

School of Electronics & Electrical Engineering, Dankook University, Yongin 16890, Republic of Korea; kdh4703@dankook.ac.kr (D.-H.K.); kms0814kk@dankook.ac.kr (M.-S.K.)
* Correspondence: ljs@dankook.ac.kr

Abstract

This paper proposes a full-speed range control method for an induction motor (IM) in railway systems using a hybrid-active neutral point clamped (HANPC) inverter. In railway systems, the demand for improving the efficiency of power semiconductors increases. Therefore, this paper proposes an IM control method for the railway system that utilizes an HANPC inverter to minimize switching losses and current harmonics. Additionally, this paper analyzes the control methods for different driving regions based on the motor's speed, including neutral point voltage balancing compensation, indirect vector control, and field weakening control. Additionally, this paper utilizes synchronous pulse width modulation (PWM) methods to improve the railway system's control performance. The proposed method's validity and feasibility are verified through the experimental results using a high-power inverter driving a 390 kW IM.

Keywords: full-speed range; railway system; HANPC inverter; induction motor; high-power motor drives

1. Introduction

The two-level inverter based on Si-IGBT is used in high-power, high-voltage railway systems. However, as the demand for improving the efficiency of power semiconductors in railway systems increases, studies of the power conversion systems have been conducted [1–5]. Compared to the two-level inverter, the multi-level inverter has a smaller voltage rating for each power semiconductor and lower switching losses at the same switching frequency [6–8]. In addition, since the number of output voltage levels can be increased, the current harmonics are improved compared to those of a two-level inverter. The three-level neutral-point-clamped (NPC) inverter, one of the multi-level inverters, can reduce the voltage rating for each power semiconductor in half compared to a two-level inverter and has the characteristic of increasing the level of the output voltage due to its structure connected to the DC-link neutral point. However, due to a non-zero average neutral-point current arising from asymmetric redundant-state selection, differences in capacitor ESR/ESL, and dead-time-induced freewheeling, this neutral-point connection structure may lead to voltage imbalance, which distorts the inverter's output voltage and increases current harmonics. As a result, switching devices may experience elevated electrical stress, potentially leading to catastrophic failure. To prevent these problems, a neutral point voltage balancing method must be applied [9–15]. In addition to the voltage imbalance problem, the NPC inverter has the disadvantage of loss and junction temperature imbalances in each switching device [16]. For this reason, research has been conducted

Check for updates

Academic Editor: Giovanni Lutzemberger

Received: 8 September 2025
Revised: 27 January 2026
Accepted: 6 February 2026
Published: 9 February 2026

Copyright: © 2026 by the authors. Licensee MDPI, Basel, Switzerland. This article is an open access article distributed under the terms and conditions of the Creative Commons Attribution (CC BY) license.

on the hybrid-active neutral point clamped (HANPC) inverter, which can apply various modulation techniques and optimize loss distribution according to these techniques [16–20]. The HANPC inverter is a topology that utilizes two switching devices (Si-IGBT and SiC-MOSFET), unlike the active neutral point clamped (ANPC) inverter, which employs only one switching device. This paper utilizes the HANPC inverter, which features four Si-IGBTs and two SiC-MOSFETs for each phase, as shown in Figure 1. Additionally, this paper employs the long-loop modulation technique to maximize loss reduction and resolve the loss imbalance between switching devices.

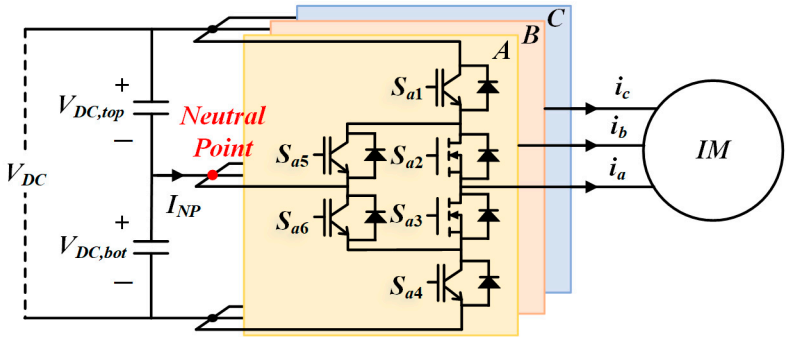


Figure 1. HANPC inverter topology.

The control of electric motors in railway systems is essential to achieving efficient and reliable operation. Railway systems operate through speed profiles: acceleration, coasting, and regenerative braking. The acceleration operation refers to the region where the motor operates from zero to maximum speed, with power being transferred from the inverter to the motor. As a result, the motor's speed increases. The acceleration operation can be divided into the magnetization region, the constant torque region, and the constant power region. The induction motor (IM) must be magnetized to generate the magnetic field for efficient torque production. When magnetizing the IM, a flux delay occurs due to the rotor time constant, representing the time required for the rotor current to respond to changes in the magnetic field. Therefore, the magnetization region is selected for a period of sufficient consideration of the rotor time constant [21,22]. In the constant torque region, torque current is applied through vector control to generate torque, increasing the motor speed [23–26]. The constant torque region is maintained until the inverter reaches its maximum output voltage. To operate the motor beyond its rated speed, limiting the back electromotive force (EMF) generated by the motor is essential. Therefore, the back EMF of the motor can be limited through field weakening control, which reduces the flux as the speed increases [27–31]. By implementing field weakening control, the inverter's output voltage remains constant, and the current flows consistently, allowing the motor to generate the required torque as the speed increases. Therefore, the region where field weakening control is applied is the constant power region, where the inverter's output power remains constant even as the speed increases. The coasting operation refers to the state where the motor is not supplied with power, and the railway continues to move only due to its kinetic energy or motion inertia. During coasting operation, torque current is not applied to the motor, but magnetization current is continuously applied to ensure control stability during the transition to regenerative braking operation. The regenerative braking operation refers to the region where the motor operates as a generator, transferring power from the motor to the inverter and thereby decelerating the motor's speed. The regenerative braking operation can be divided into the constant torque region and the constant power region, similar to the acceleration operation. Since the back EMF is maintained in the constant power region by field weakening control, the magnetization current gradually

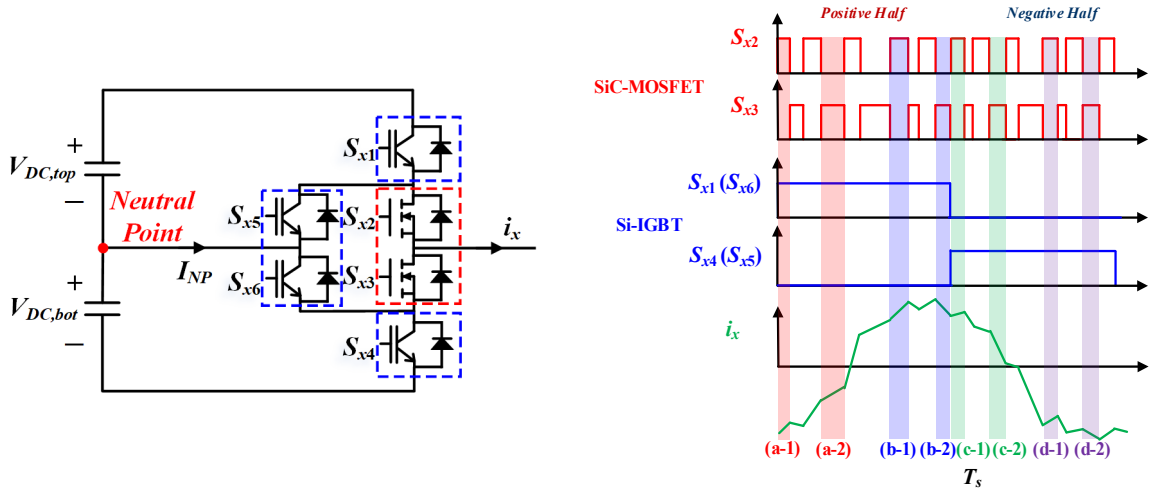
increases as speed decreases until it reaches the rated value. In the constant torque region, torque is applied to reduce the motor's speed, and this region is maintained until the speed reaches zero.

This paper proposes a control method for the IM in railway systems by applying an HANPC inverter to reduce switching losses and current harmonics. Based on motor speed, this paper analyzes the essential control methods used in various operating regions, including acceleration, coasting, and regenerative braking. In addition, this paper applies neutral point voltage balancing compensation to ensure balanced voltage across the top and bottom capacitors of the DC-link [13] and a synchronous pulse width modulation (PWM) method to eliminate output voltage imbalance [32]. Additionally, to compensate for the inverter nonlinearity, the dead-time compensation method [20] and the time delay compensation method [33] are used. The feasibility of the proposed method was verified through the experimental results on a high-power inverter driving a 390 kW IM.

2. Control Method of HANPC Inverter

2.1. Long-Loop Modulation Method for HANPC Inverter

Figure 2a shows one phase of the HANPC inverter used in this paper. The path connected to each phase of the motor consists of two SiC-MOSFETs (S_{x2} and S_{x3}, $x = a, b, c$), while the remaining switches are composed of four Si-IGBTs (S_{x1}, S_{x4}, S_{x5}, and S_{x6}). Figure 2b shows the switching waveforms when applying the long-loop modulation method. As shown in Figure 2b, the two SiC-MOSFETs perform high-speed switching operations, while the four Si-IGBTs carry clamping operations. Additionally, S_{x2} and S_{x3} operate in a complementary switching, whereas S_{x1} and S_{x6}, as well as S_{x4} and S_{x5}, always operate simultaneously.



(**a**) (**b**)

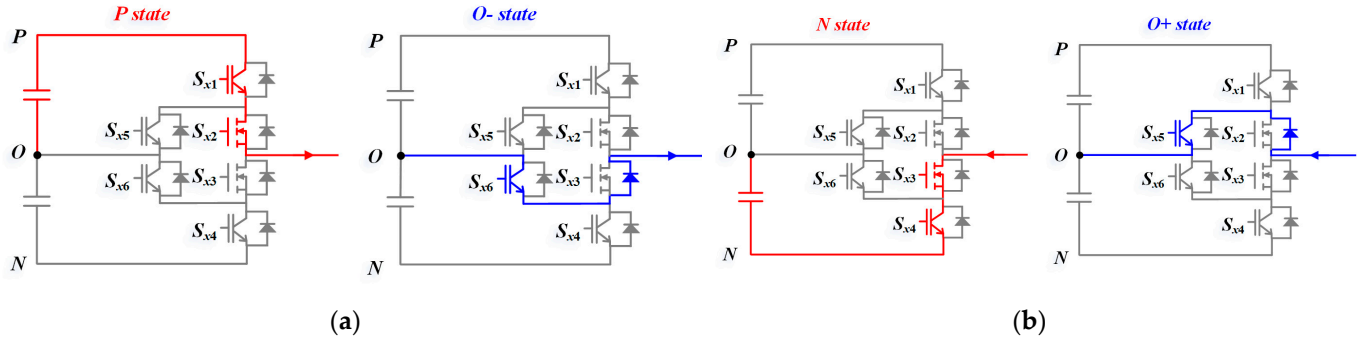
Figure 2. Long-loop modulation method in HANPC inverter: (**a**) one phase of the HANPC inverter; (**b**) switching waveforms and current waveforms when applying the long-loop modulation method.

Due to the switch connected to the neutral point path of the HANPC inverter, the inverter's output voltage has three different voltage levels ($0.5V_{DC}$, 0, and $-0.5V_{DC}$). Table 1 shows the switching state of the HANPC inverter according to the output voltage.

Table 1. Switching states of the long-loop modulation method in the HANPC inverter.

Switching State	Voltage Level	S_{x1}	S_{x2}	S_{x3}	S_{x4}	S_{x5}	S_{x6}
P state	$0.5V_{DC}$	1	1	0	0	0	1
O- state	0	1	0	1	0	0	1
O+ state	0	0	1	0	1	1	0
N state	$-0.5V_{DC}$	0	0	1	1	1	0

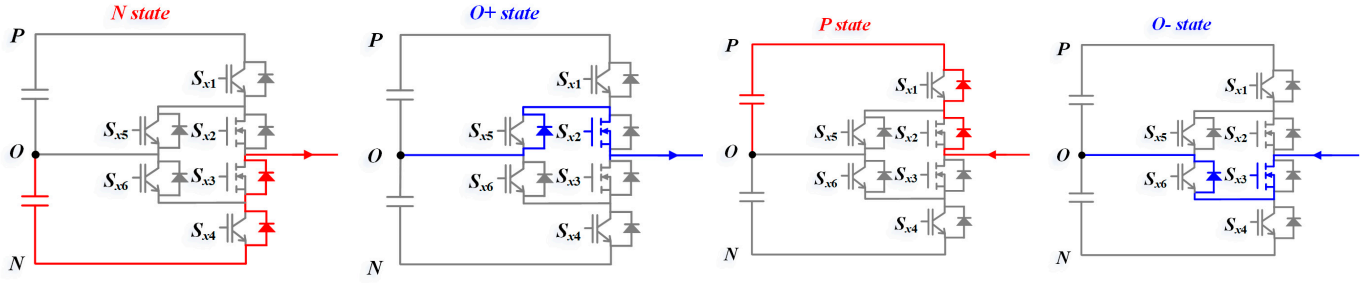
Based on Table 1, Figure 3 shows the current flow of the HANPC inverter for a power factor of 1, depending on the direction of the current. In Figure 3a, as the current flows in the positive direction, the switching states are determined as P state and O- state, and the inverter's output voltage is $0.5V_{DC}$ and 0V, respectively. Contrarily, as shown in Figure 3b, when the current flows in the negative direction, the switching states are determined as N state and O+ state, and the inverter's output voltage is $-0.5V_{DC}$ and 0V, respectively.



(**a**) (**b**)

Figure 3. Current flow of the HANPC inverter for a power factor of 1: (**a**) current flows in the positive direction; (**b**) current flows in the negative direction.

Figure 4 shows the current flow of the HANPC inverter when the power factor is -1, depending on the direction of the current. In contrast to the case with a power factor of 1, when the power factor is -1 and the current flows in the positive direction, the switching states are determined as N state and O+ state, as shown in Figure 4a. In addition, when the current flows in the negative direction, the switching states are determined as the P state and O- state, as shown in Figure 4b.



(**a**) (**b**)

Figure 4. Current flow of the HANPC inverter for a power factor of -1: (**a**) current flows in the positive direction; (**b**) current flows in the negative direction.

As shown in Figure 2b, the phase current (i_x) varies according to the switching operation of the HANPC inverter. When the phase current flows in the positive direction, regions (b-1) and (b-2) correspond to the P state and O- state, respectively, as illustrated

in Figure 3a. Conversely, when the phase current flows in the negative direction, regions (d-1) and (d-2) correspond to the N state and O+ state, respectively, as shown in Figure 3b. In addition, regions (a-1) and (a-2) correspond to the O+ state and N state, respectively, as illustrated in Figure 4b, while regions (c-1) and (c-2) correspond to the O- state and P state, respectively, as shown in Figure 4a. Therefore, the current waveform in Figure 2b can be directly mapped to the switching states shown in Figures 3 and 4, providing a clear representation of how the current changes according to each switching condition of the HANPC inverter.

As shown in Figures 3 and 4, the switching loop is elongated for all HANPC inverter operations when using the long-loop modulation method. When the switching loop is elongated, the influence of stray inductance increases. However, the advantage of using the long-loop modulation is that it can resolve the switching device loss imbalance [16].

2.2. Neutral Point Voltage Balancing Compensation

Due to the characteristics of the three-level inverter with a neutral point current path, the unbalanced voltage between each DC-link capacitor (ΔV_{DC}) occurs. ΔV_{DC} results in the following problems: (1) the inverter's output voltage becomes distorted, leading to an increase in current harmonics, and (2) the switching devices are subjected to elevated electrical stress, which could potentially lead to catastrophic failure [9–15]. Therefore, to solve these problems, it is necessary to compensate for ΔV_{DC}.

ΔV_{DC} can be analyzed by considering two cases based on the direction of the neutral point current (I_{NP}). When I_{NP} flows toward the neutral point, the top side DC-link capacitor voltage ($V_{DC,top}$) decreases, while the bottom side DC-link capacitor voltage ($V_{DC,bot}$) increases. In contrast, when I_{NP} flows out of the neutral point, $V_{DC,top}$ increases, while $V_{DC,bot}$ decreases. I_{NP} can be calculated using the duty cycle(d_x) of each phase and i_x, and is expressed as follows:

$$I_{NP} = -(|d_a|i_a + |d_b|i_b + |d_c|i_c). \tag{1}$$

In addition, ΔV_{DC} can be expressed as follows:

$$\Delta V_{DC} = \frac{1}{C_{DC}} \int (-I_{NP}) dt = \frac{1}{C_{DC}} \int -(|d_a|i_a + |d_b|i_b + |d_c|i_c) dt, \tag{2}$$

where C_{DC} is the DC-link capacitance.

To minimize ΔV_{DC}, this paper employs a PI controller-based neutral point voltage balancing compensation [13], which combines time delay components and an antiwindup loop, as shown in Figure 5.

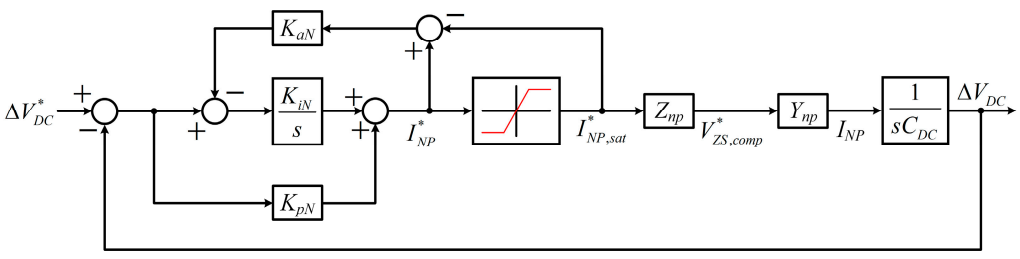


Figure 5. Block diagram of the neutral point voltage balancing compensation.

As shown in Figure 5, using the difference between ΔV_{DC} and the unbalanced voltage reference (ΔV^*_{DC}), the PI controller outputs the neutral point reference current (I^*_{NP}), where K_{iN} and K_{pN} are the integral gain and proportional gain of the neutral point voltage balancing compensation, respectively. To implement an antiwindup loop, a limiter is required. I^*_{NP} is passed through a limiter to produce the saturated neutral point reference

current ($I^*_{NP,sat}$), which is used for antiwindup control, where K_{aN} is the antiwindup gain. The $I^*_{NP,sat}$ is then processed via the neutral point impedance (Z_{np}) to obtain the zero sequence reference voltage ($V^*_{ZS,comp}$), and multiplying $V^*_{ZS,comp}$ by the neutral point admittance (Y_{NP}) to calculate I_{NP}.

3. Modeling of Induction Motor

Induction motors (IM) require high-performance control in various applications, and instantaneous torque control is often used in such fields. To achieve instantaneous torque control, a coordinate transformation is applied to the three-phase AC current, generating flux component current and torque component current, which rotate with the rotor flux linkage angle at a 90° phase difference.

The flux component current is typically set as the d-axis stator current in the synchronous reference frame (i^e_{ds}), while the torque component current is set as the q-axis stator current in the synchronous reference frame (i^e_{qs}). The corresponding d-q axis stator voltages in the synchronous reference frame (v^e_{ds} and v^e_{qs}), generated by i^e_{ds} and i^e_{qs}, can be expressed as follows:

$$\begin{aligned} v^e_{ds} &= R_s i^e_{ds} + \frac{d\lambda^e_{ds}}{dt} - \omega_e \lambda^e_{qs} \\ v^e_{qs} &= R_s i^e_{qs} + \frac{d\lambda^e_{qs}}{dt} + \omega_e \lambda^e_{ds}, \end{aligned} \tag{3}$$

where R_s is the stator resistance of the induction motor, ω_e is the electrical angular speed, λ^e_{ds} is the d-axis stator flux linkage, and λ^e_{qs} is the q-axis stator flux linkage. λ^e_{ds} and λ^e_{qs} can be expressed as follows:

$$\begin{aligned} \lambda^e_{ds} &= L_s i^e_{ds} + L_m i^e_{dr} \\ \lambda^e_{qs} &= L_s i^e_{qs} + L_m i^e_{qr}, \end{aligned} \tag{4}$$

where L_s is the stator inductance, L_m is the mutual inductance, i^e_{dr} and i^e_{qr} are the d-axis rotor current in the synchronous reference frame and the q-axis rotor current in the synchronous reference frame, respectively. In addition, the d-q axis rotor voltages in the synchronous reference frame (v^e_{dr} and v^e_{qr}) are expressed as follows:

$$\begin{aligned} v^e_{dr} &= R_r i^e_{dr} + \frac{d\lambda^e_{dr}}{dt} - (\omega_e - \omega_r)\lambda^e_{qr} \\ v^e_{qr} &= R_r i^e_{qr} + \frac{d\lambda^e_{qr}}{dt} + (\omega_e - \omega_r)\lambda^e_{dr}, \end{aligned} \tag{5}$$

where R_r is the rotor resistance, ω_r is the mechanical angular speed, λ^e_{dr} is the d-axis rotor flux linkage, and λ^e_{qr} is the q-axis rotor flux linkage. λ^e_{dr} and λ^e_{qr} can be expressed as follows:

$$\begin{aligned} \lambda^e_{dr} &= L_r i^e_{dr} + L_m i^e_{ds} \\ \lambda^e_{qr} &= L_r i^e_{qr} + L_m i^e_{qs}, \end{aligned} \tag{6}$$

where L_r is the rotor inductance.

In the same way as (3)~(6), the torque of IM (T_e) can be expressed in the d-q axis coordinate system as follows:

$$T_e = \frac{P}{2}\frac{3}{2}\frac{L_m}{L_r}\left(\lambda^e_{dr} i^e_{qs} - \lambda^e_{qr} i^e_{ds}\right), \tag{7}$$

where P is the number of poles.

4. Control Method of Induction Motors in the Full Speed Range

In electric motor drive systems, the motor's operating mode is determined by the direction of power transfer, which in railway systems corresponds to the torque direction of the motor. When the motor generates positive torque, it is defined as an acceleration operation. Conversely, when the motor generates negative torque, it is defined as a regenerative

braking operation. Additionally, if the motor neither generates torque nor transfers power, it is defined as a coasting operation. This section analyzes the control methods applied to each operation in railway systems.

In practical railway traction systems, the rate of change in speed is constrained by the large mechanical inertia and control limits and the torque reference is ramp-limited by the traction control to reduce mechanical stress, wheel slip, and passenger discomfort [34–36]. Therefore, the system variables vary slowly with respect to time, allowing the time-varying components to be neglected. Under this assumption, the steady-state analysis is conducted in this section to examine the control methods applied to each operation.

4.1. Acceleration Operation in Railway System

The acceleration operation is defined when the IM increases its speed from zero to the maximum value by receiving power from the inverter. The acceleration operation is divided into three regions: the magnetization region, the constant torque region, and the constant power region. In the magnetization region, the magnetizing current is supplied to the IM's rotor to generate the rotor flux for operation. In the constant torque region, torque control is used to ensure that the IM generates a maximum torque. As torque is produced, the IM speed increases, causing the back electromotive force (EMF) to rise accordingly. The back EMF continues to increase until it reaches the inverter's maximum output voltage. The operation transitions to the constant power region when the back EMF equals the inverter's maximum output voltage. In this region, field weakening control is applied to maintain the back EMF while speed increases. Additionally, the IM is supplied with the maximum current to maximize torque output as speed increases.

Figure 6 shows the torque-speed (T-N) curve of the IM. In the constant torque region, vector control is applied to generate the demanded torque. As shown in Figure 6, the IM accelerates under positive torque, which increases the v_{smag}. When v_{smag} reaches v_{smax}, the IM transitions to the constant power region. In the constant power region, even as the IM's speed increases, the IM operates to satisfy both v_{smax} and i_{smax}, maintaining a consistent v_{smag} and i_s by applying the field weakening control. As a result, the power supplied to the IM remains consistent, resulting in constant power operation.

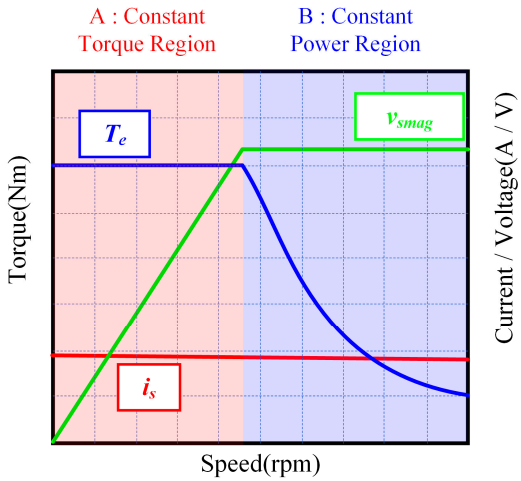


Figure 6. Torque-speed (T-N) curve of the IM.

4.1.1. Rotor Flux-Oriented Vector Control (RFOVC) in the Acceleration Operation

RFOVC, a vector control method for instantaneous torque control, controls the slip angular speed (ω_{sl}) of the IM to distribute the stator current (i_s) into the desired flux and

torque component currents. In RFOVC, since the rotor flux linkage is aligned with the d-axis, ${\lambda^e}_{qr}$ does not occur. Therefore, ${v^e}_{qr}$ can be expressed as follows:

$$v^e_{qr} = R_r i^e_{qr} + (\omega_e - \omega_r)\lambda^e_{dr} = 0. \tag{8}$$

Using (8), ω_{sl} can be expressed as follows:

$$\omega_{sl} = \omega_e - \omega_r = -\frac{R_r i^e_{qr}}{\lambda^e_{dr}}. \tag{9}$$

In (9), when ${i^e}_{qr}$ is converted to ${i^e}_{qs}$ with the time-varying component of ${\lambda^e}_{dr}$ neglected, it can be expressed as follows:

$$\omega_{sl} = \frac{R_r L_m}{L_r}\frac{i^e_{qs}}{\lambda^e_{dr}} = \frac{R_r}{L_r}\frac{i^e_{qs}}{i^e_{ds}}(\lambda^e_{dr} = L_m i^e_{ds}). \tag{10}$$

In RFOVC, the d-axis stator reference current (${i^{e^*}}_{ds}$) and the q-axis stator reference current (${i^{e^*}}_{qs}$) in steady state conditions are defined as follows:

$$\begin{array}{c} i^{e*}_{ds} = \frac{\sqrt{2}v_{LL,rated}/\sqrt{3}}{\sqrt{R_s + (\omega_{rated}L_s)^2}} = \frac{\lambda^{e*}_{dr}}{L_m} \\ i^{e*}_{qs} = \frac{T^*_e}{\frac{3}{2}\frac{P}{2}\frac{L_m}{L_r}\lambda^{e*}_{dr}}, \end{array} \tag{11}$$

where $v_{LL,rated}$ is the rated value of the line-to-line voltage, ω_{rated} is the rated electrical angular speed, ${\lambda^{e^*}}_{ds}$ is the d-axis stator reference flux linkage, and ${T^*}_e$ is the torque reference.

In the magnetization region, the flux component current is applied to generate the flux necessary for torque production in the IM. Since ${i^e}_{qs}$ is not applied, the IM remains in a stop condition during this period. ${i^e}_{ds}$ used during the magnetization time flow as ${i^{e^*}}_{ds}$, and the time constant (T_r) of the IM determines the magnetization time. T_r of the IM can be expressed as follows:

$$T_r = \frac{L_r}{R_r}. \tag{12}$$

In the constant torque region, ${i^e}_{qs}$ flows through the IM as ${i^{e^*}}_{qs}$ is applied, which is calculated by ${T^*}_e$, generating the IM's output torque. As the output torque is generated, the IM accelerates, causing a change in the position of the rotor flux linkage (θ_e). In RFOVC, θ_e is expressed using ω_r obtained from the speed sensor and ω_{sl} generated from ${i^{e^*}}_{ds}$ and ${i^{e^*}}_{qs}$ as follows:

$$\theta_e = \int \omega_e dt = \int (\omega_r + \omega_{sl})dt. \tag{13}$$

The constant torque region is maintained until the inverter's output voltage reaches the limit of the inverter's output voltage.

4.1.2. Field Weakening Control in the Acceleration Operation

In the constant power region, IM's torque decreases as speed increases to maintain output power. With increasing the speed of an IM, the IM's back EMF rises and can exceed the inverter's maximum output voltage. If the IM's required voltage exceeds the inverter's maximum output voltage, the inverter loses the ability to supply the torque-producing current with stability. Therefore, the back EMF must be maintained below the inverter's output voltage to achieve stable control of the current required for IM's torque generation, which is achieved through field weakening control. Since the stator resistance drop is

negligible in large-capacity IMs, $v^e{}_{ds}$ and $v^e{}_{qs}$ in steady state conditions can be expressed as follows:

$$\begin{aligned} v^e_{ds} &= -\omega_e \sigma L_s i^e_{qs} \\ v^e_{qs} &= \omega_e \sigma L_s i^e_{ds} + \omega_r \frac{L_m}{L_r} \lambda^e_{dr} = \omega_e L_s i^e_{ds}, \end{aligned} \tag{14}$$

where σ is the leakage factor and it can be expressed as follows:

$$\sigma = 1 - \frac{L_m^2}{L_s L_r}. \tag{15}$$

Using (14), the stator voltage limit condition (v_{smax}) can be expressed as follows:

$$v^{e2}_{ds} + v^{e2}_{qs} = (\omega_e \sigma L_s i^e_{qs})^2 + (\omega_e L_s i^e_{ds})^2 \leq v^2_{smax}. \tag{16}$$

In addition, the stator current limit condition (i_{smax}) for applying the maximum torque to the IM can be expressed as follows:

$$i^{e2}_{ds} + i^{e2}_{qs} \leq i^2_{smax}. \tag{17}$$

Using (16) and (17), the operable region of the IM is represented in Figure 7.

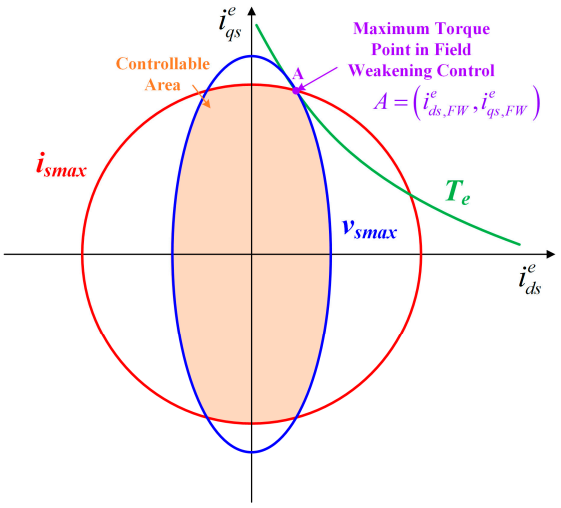


Figure 7. Operable region of the IM under field weakening control.

As shown in Figure 7, the IM can operate only within the region that satisfies both v_{smax} and i_{smax}. Maximizing torque output and satisfying these limit conditions requires the control to be performed through the current combination of the intersection of the voltage limit ellipse and the current limit circle. This intersection corresponds to point A in Figure 7; commanding the d- and q-axis currents ($i^e{}_{ds,FW}$ and $i^e{}_{qs,FW}$) at point A enables field weakening control of the IM while respecting both constraints.

Figure 8 shows the change in the operating point of the IM with an increase in speed, where field weakening control is applied to maintain v_{smax}. As shown in Figure 8, as the speed of the IM increases, the region of the IM's voltage limit ellipse decreases. Consequently, $i^e{}_{ds}$ decreases, and $i^e{}_{qs}$ increases due to i_{smax}. In field weakening control, $i^{e*}{}_{ds}$ and $i^{e*}{}_{qs}$ can be expressed as follows:

$$\begin{aligned} i^{e*}_{ds} &= \sqrt{\frac{(v_{smax}/\omega_e)^2 - (\sigma L_s i_{smax})^2}{L_s^2 - \sigma L_s^2}} \\ i^{e*}_{qs} &= \sqrt{i^2_{smax} - i^{e*2}_{ds}}. \end{aligned} \tag{18}$$

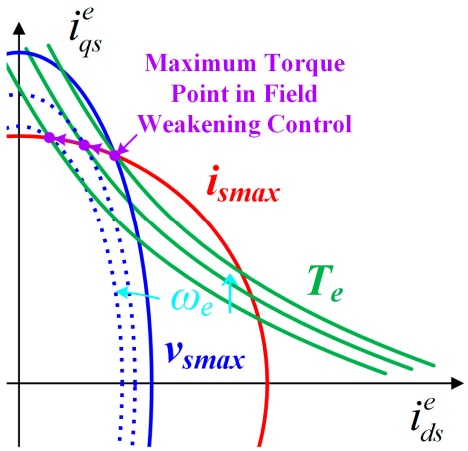


Figure 8. Operating point variation with increasing speed during field weakening control.

4.2. Coasting Operation in the Railway System

Coasting in an electric railway system is an operation that reduces energy consumption and improves operational efficiency by discontinuing the power supply, allowing the railway to run by inertia after reaching an operating speed. During coasting operation, the inverter discontinues the delivery of active propulsion power but still supplies power to cover the inverter and motor losses, as well as to maintain the magnetizing current. Consequently, the electromagnetic torque becomes zero, and the motor rotates by inertia, generating a back-EMF proportional to its rotational speed. The inverter regulates the voltage as much as the back EMF produced by the rotating motor to prevent unintended power flow, while the magnetizing current is maintained to stabilize the motor's magnetic flux.

4.3. Regenerative Braking Operation in Railway System

The regenerative braking operation decelerates the IM by applying negative torque and transferring power from the IM to the inverter. Since the regenerative braking operation begins after the coasting operation, the regenerative braking operation starts at a speed higher than the rated speed of the IM. Therefore, as in the acceleration operation, field weakening control is applied during the regenerative braking operation to maintain v_{smax} since the back EMF of the IM can exceed the output voltage of the inverter. During the field weakening control in regenerative braking operation, the back EMF is maintained as the motor speed decreases, which increases ${i^e}_{ds}$. This increase starts the remagnetization process in the IM. However, due to the first-order delay response of ${\lambda^e}_{dr}$ to the change in ${i^e}_{ds}$, the ${\lambda^e}_{dr}$ does not generate immediately, which may lead to a degradation in the system's dynamic performance.

Considering the first-order lag response, ${\lambda^e}_{dr}$ can be expressed as follows:

$$\lambda^e_{dr} = L_m i^e_{ds}(1 - e^{-t/T_r}). \tag{19}$$

Using (19), the feedforward voltage of the current controller (${v^e}_{ds,ff}$ and ${v^e}_{qs,ff}$) can be expressed as follows:

$$\begin{aligned} v^e_{ds,ff} &= -\omega_e \sigma L_s i^e_{qs} \\ v^e_{qs,ff} &= \omega_e \sigma L_s i^e_{ds} + \omega_r \frac{L_m^2}{L_r} i^e_{ds}\left(1 - e^{-\frac{t}{T_r}}\right). \end{aligned} \tag{20}$$

Considering the flux delay in the feedforward voltage, the error in the stator voltage caused by the flux delay is reduced, thereby improving the dynamic performance during field weakening control. During field weakening control in the regenerative braking region, ${i^e}^*_{ds}$ and ${i^e}^*_{qs}$ are calculated as in the acceleration region, as expressed in (18). In addition,

when the IM reaches the constant torque region due to a decrease in speed, torque control is performed using RFVOC, similarly to the acceleration region, until the IM comes to a stop.

4.4. Synchronous Pulse Width Modulation Method

In synchronous PWM, the switching frequency is defined by multiplying the fundamental frequency by a specific integer, as shown in Figure 9. The number of output voltage pulses generated during one cycle of the fundamental waveform corresponds to this integer. For the waveform to retain half-wave, quarter-wave, and three-phase symmetry, the number of pulses should preferably be selected as an odd multiple of three [32]. The number of pulses (N) is expressed as follows:

$$N = 3(2m - 1) \quad (m = 1,\ 2,\ 3,\ \cdots). \tag{21}$$

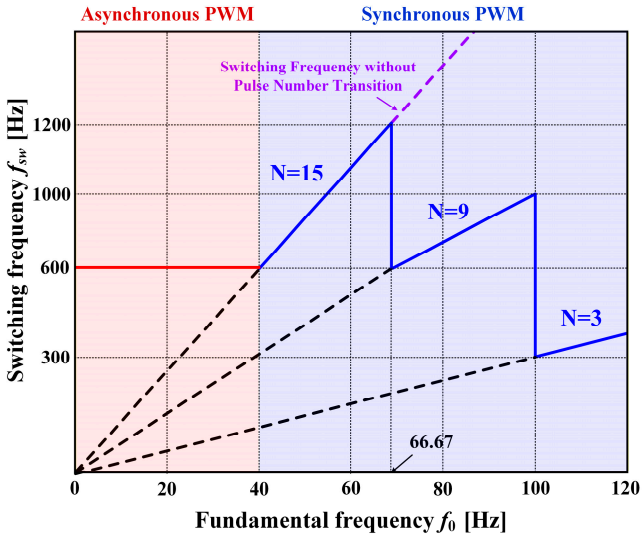


Figure 9. Switching frequency variation according to pulse number and fundamental frequency.

In addition, the switching frequency of the synchronous PWM (f_{sw}) can be expressed as follows:

$$f_{sw} = N \cdot f_s, \tag{22}$$

where f_s is the electrical frequency of the motor, since f_s varies with the motor speed, the f_{sw} in (22) also changes accordingly.

As f_{sw} varies, the control period (T_s) changes accordingly and is expressed as follows:

$$T_s = \frac{1}{f_{sw}} = \frac{1}{N \cdot f_s}. \tag{23}$$

In low switching frequency (high-power) operation with synchronous PWM, changing N abruptly shifts T_s. It generates a synchronization phase error (φ_{err}) between the reference and actual sampling, which degrades the current controller's performance and stability. Therefore, in this paper, the proposed method in [32] is used to compensate for φ_{err}.

4.5. Inverter Nonlinearity Compensation Methods

Inverter nonlinearity causes output voltage distortion, and the harmonics in the output currents increase accordingly. Additionally, the reference voltage of the inverter would differ from the actual output voltage to the IM. The difference would severely degrade the control performance of the motor drive system. To compensate for the inverter nonlinearity, this paper employs the dead-time compensation method proposed in [20] and the time-delay compensation method proposed in [33].

4.5.1. Dead-Time Compensation Method

In [20], to compensate for voltage nonlinearity, the feedforward voltage is calculated by considering each conducting device pair and switching state. For each conducting device pair and switching state, the average voltage deviation over one PWM period is computed from device nonidealities (dead-time, conduction drops, and commutation delays) together with the system's power factor angle. The resulting per-phase compensation voltage is injected into the stator reference voltages before modulation, which reduces current distortion and enhances current loop operation across various operating conditions. The compensation voltage of the voltage nonlinearity ($\Delta v_{xs,h}$) is expressed as follows:

$$\begin{aligned} &\Delta v_{xs,h} = -\tfrac{4}{\pi}\left|\Delta v_{xn,k}\right|\textstyle\sum_{k=1,3,5,\cdots}^{13}\left\{\tfrac{1}{k}sink\left(\theta_e-\theta_x-\theta_{pf}\right)\right\}\cdot sign(pf), \\ &\left\{\theta_x(a,b,c)=\left(0,\tfrac{2}{3}\pi,-\tfrac{2}{3}\pi\right)\right\},\quad sign(pf)=\begin{cases}1(0\le pf\le 1)\\ -1(-1\le pf\le 0),\end{cases}\end{aligned} \tag{24}$$

where $\Delta v_{xn,k}$ is the average voltage errors for one sampling period, and θ_{pf} is the phase difference between the phase voltage and current. θ_{pf} varies depending on the changes in torque and the back EMF caused by variations in the motor speed of the IM. $\Delta v_{xn,k}$ can be expressed as follows:

$$\Delta v_{xn,k}=\begin{cases}2V_{ce}+\frac{V_{DC}}{2}\cdot\frac{T_d}{T_s}\cdot sign(i_x) & (in\ 1^{st}\ and\ 3^{rd}\ quadrants)\\ 2V_d+\frac{V_{DC}}{2}\cdot\frac{T_d}{T_s}\cdot sign(i_x) & (in\ 2^{nd}\ and\ 4^{th}\ quadrants)\end{cases}, \tag{25}$$

where V_{ce} is the on-state voltage of the IGBT and V_d is the forward on-state voltage of the anti-parallel diode of the IGBT.

4.5.2. Time-Delay Compensation Method

In most industrial motor drives and power converters, the current controller and PWM generator are implemented on a digital processor, resulting in a time delay. In the digital unit, the calculated output voltage has a time delay of $1T_s$. Additionally, a time delay of $0.5T_s$ is generated due to the characteristic of SVPWM, where the reference voltage vector is located at the midpoint of the sampling period [33]. In [33], since the magnitude and phase errors of the output voltage caused by the time delay vary with the motor speed, the magnitude and phase of the output voltage were compensated by multiplying the output of the current controller by the compensation function ($K(\omega_e, T_s)$). $K(\omega_e, T_s)$ can be expressed as follows:

$$K(\omega_e,T_s)=\frac{2}{\omega_e T_s}sin\left(\frac{\omega_e T_s}{2}\right)e^{j(1.5T_s\omega_e)} \tag{26}$$

Figure 10 shows the entire block diagram that includes the synchronous PWM. In the acceleration operation, when v_{smag} is smaller than v_{smax}, the IM is controlled based on (11), resulting in acceleration. As the IM speed increases, the fundamental frequency of the inverter output voltage increases. When f_{sw}, which is defined in (22), reaches the switching frequency of the asynchronous PWM (f_{async}), the control transitions to synchronous PWM. On the other hand, when v_{smag} exceeds v_{smax}, the field-weakening controller is activated, and the IM is controlled using (18). As the IM continues to accelerate and reaches the motor's maximum speed, $i^{e^*}_{qs}$ becomes zero for forward coasting operation. During the regenerative braking operation, the field-weakening control is maintained as the IM decelerates. When v_{smag} becomes smaller than v_{smax}, the IM is controlled based on (11), and the IM decelerates. When f_{sw}, as defined in (22), decreases with IM speed and reaches f_{async},

the control transitions to asynchronous PWM. The IM continues to decelerate until it comes to a stop.

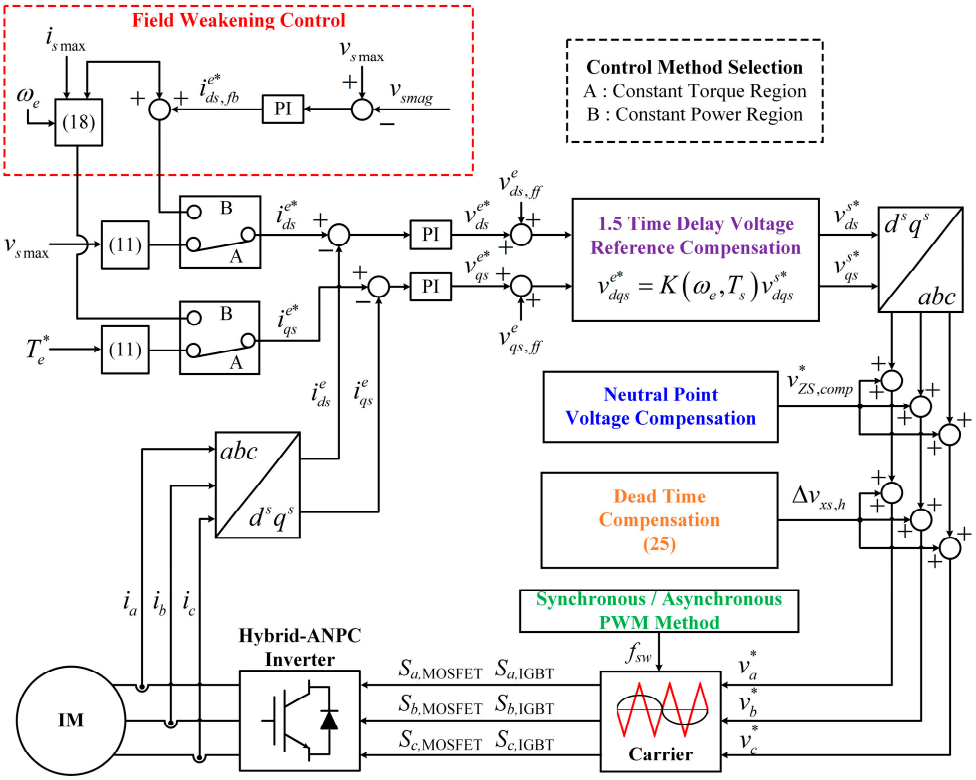


Figure 10. Entire block diagram.

5. Experimental Results

To verify the validity of the proposed method, an experimental setup, as shown in Figure 11, was constructed using an induction motor with the parameters shown in Table 2. The inverter was constructed with one 1700V/1400A SI IGBT SKM1400GB17R8 module and two 1700V/650A SIC MOSFET CAB650M17HM3 modules in each leg. The control method was implemented using a Texas Instruments TMS320F28377 microcontroller. The whole DC-link capacitance was 2400μF; f_{sw} in the asynchronous PWM was set to 600 Hz, and the deadtime (T_{dead}) was set to 12μs. In addition, T^*_e was set to 1500 Nm in the acceleration operation and 857 Nm in the regenerative braking operation. Large mechanical inertia and control constraints prevent rapid speed changes in railway traction systems. To further suppress abrupt disturbances, the controller limits the torque reference with a ramp, which reduces mechanical stress, wheel slip, and passenger discomfort. As a result, the dynamic variations in the drive system are sufficiently smooth, and the experimental validation accurately reflects the actual operating characteristics of high-power traction drives [34–36].

Table 2. Motor parameters.

Parameters	Value	Parameters	Value
Stator Resistance (R_s)	0.0155 Ω	Magnetizing Inductance (L_m)	0.00784 H
Rotor Resistance (R_r)	0.02146 Ω	No. of poles (P)	6
Stator Inductance (L_s)	0.008346 H	DC-link Voltage (V_{DC})	1500 V
Rotor Inductance (L_r)	0.008346 H	Switching Frequency of Asynchronous PWM (f_{async})	600 Hz

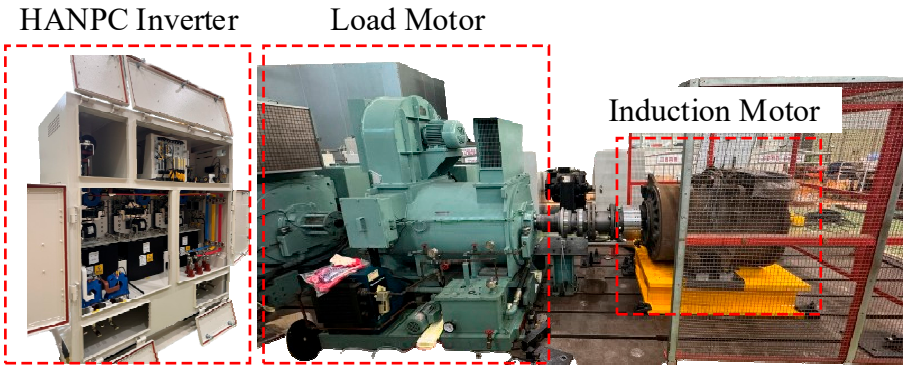


Figure 11. Inverter and motor setup.

Figure 12 shows the experimental results of the full speed range and the corresponding torque profile. In Figure 12, region A represents the constant torque region during acceleration operation. In this region, i^e_{ds} is maintained at its rated value, while i^e_{qs} is applied according to T^*_e. Region B is the constant power region in acceleration operation. As the speed increases, v_{smag} increases. To prevent v_{smag} from exceeding v_{smax}, the field weakening control is applied, resulting in a decrease in i^e_{ds}. Since the magnitude of i_s must remain constant in the constant power region, i^e_{qs} increases as i^e_{ds} decreases. Additionally, to maintain a constant output power, the torque decreases as the speed increases. Region C is the coasting operation, where i^e_{ds} remains constant and i^e_{qs} is regulated to zero to prevent torque generation by the IM. Region D is the constant power region in regenerative braking operation. In this region, as the speed decreases, the i^e_{ds} increases. In addition, i^e_{qs} increases in the negative direction to satisfy the torque profile. To prevent abrupt torque transients and to reduce sudden variations in the stator voltage during field-weakening control, i^{e*}_{qs} is applied as a ramp-down profile rather than as a step, resulting in a smooth torque response throughout Region D. Region E corresponds to the constant torque region during regenerative braking operation, where i^e_{ds} is maintained at its rated value, and i^e_{qs} is controlled according to T^*_e.

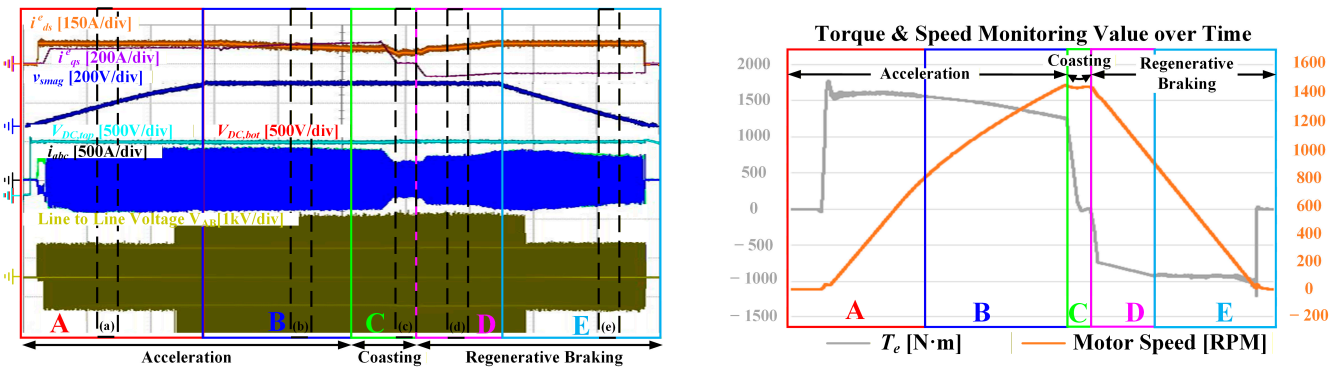


Figure 12. Experimental results of the full speed range and the corresponding torque profile: (**a**) full experimental results; (**b**) torque and speed profile.

Figure 13 shows the enlarged waveforms of the experimental results for each region in Figure 12. As shown in Figure 13a,b, i^e_{qs} is applied with a positive value to generate a positive torque in the IM. During the transition from the constant torque region to the constant power region, the magnitude of i_s remains constant. In Figure 13c, with the transition into the coasting region, i^e_{qs} is controlled to zero. Figure 13d,e shows that i^e_{qs} is applied with a negative value to generate a negative torque in the IM. Furthermore, as

shown in Figure 13, $V_{DC,top}$ and $V_{DC,bot}$ are balanced and controlled throughout the full speed range.

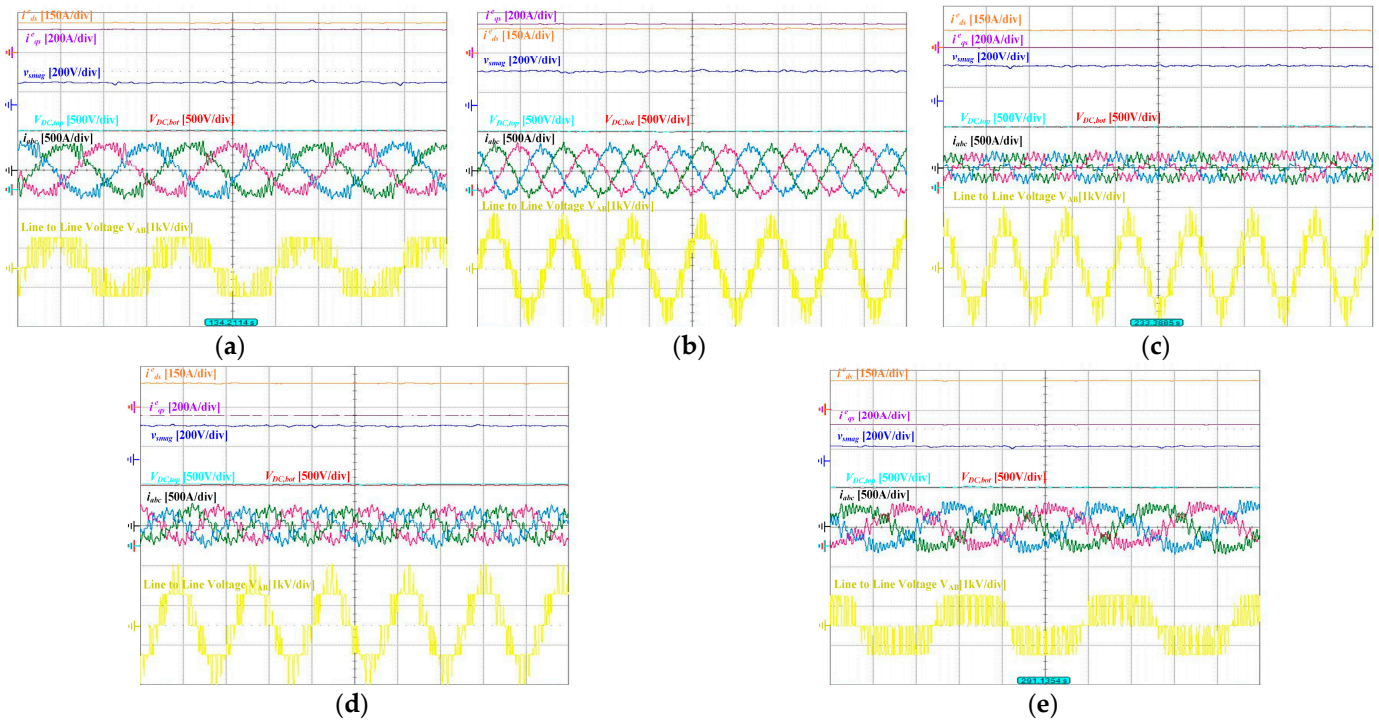


Figure 13. Enlarged waveforms of the experimental results for each region in Figure 12: (**a**) Region A; (**b**) Region B; (**c**) Region C; (**d**) Region D; (**e**) Region E.

Figure 14 shows the experimental results obtained when the synchronous PWM is applied. As shown in Figure 14, T_s varies as the control method transitions from asynchronous PWM to synchronous PWM, and φ_{err} between the reference sampling point and the actual sampling point is reduced.

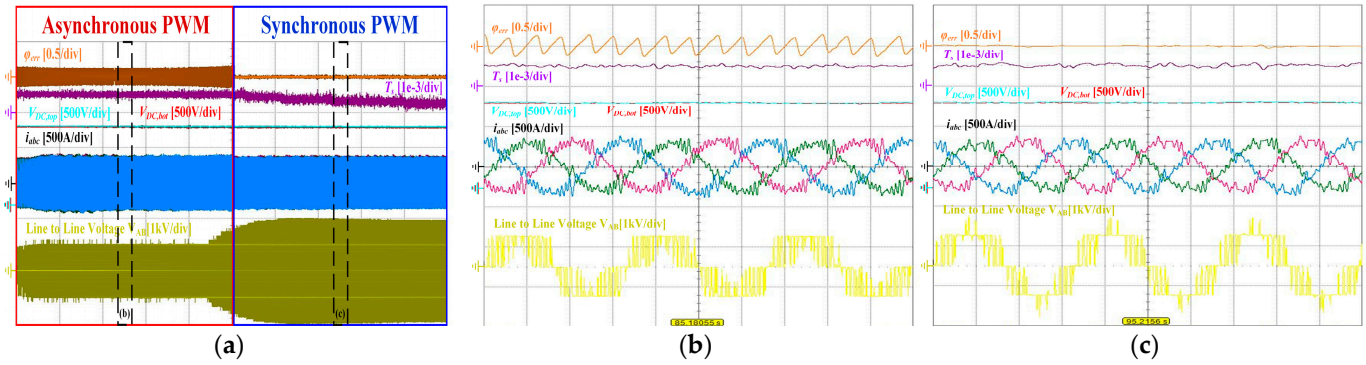


Figure 14. Experimental results with synchronous PWM applied: (**a**) full experimental result; (**b**) enlarged waveform in an asynchronous PWM; (**c**) enlarged waveform in a synchronous PWM.

6. Conclusions

This paper proposes a full-speed range control method for the induction motor (IM) used in railway systems, based on a hybrid active neutral-point clamped (HANPC) inverter. The proposed method addresses the wide speed range requirement of traction drives and the voltage imbalance inherent in HANPC inverter topologies. Railway vehicle operation can be divided into acceleration, coasting, and regenerative braking modes, each requiring an appropriate control strategy, based on the speed profile. In the proposed method,

vector control is applied to achieve full-speed range operation, while neutral-point voltage compensation and synchronous PWM are employed to enhance control performance. The validity of the proposed methods was verified through the experimental results using a high-power inverter driving a 390 kW IM. Importantly, the results confirm that the proposed approach ensures stable operation across all speed regions, improves voltage balancing, and reduces current distortion in a real-scale experimental setup of 390 kW. These highlight the applicability of the proposed method to large-capacity railway traction systems.

Author Contributions: Conceptualization, D.-H.K. and J.-S.L.; methodology, D.-H.K.; software, D.-H.K.; validation, D.-H.K., M.-S.K. and J.-S.L.; formal analysis, D.-H.K.; investigation, D.-H.K. and M.-S.K.; resources, J.-S.L.; data curation, D.-H.K. and M.-S.K.; writing—original draft preparation, D.-H.K.; writing—review and editing, D.-H.K., M.-S.K. and J.-S.L.; visualization, D.-H.K.; supervision, J.-S.L.; project administration, J.-S.L.; funding acquisition, J.-S.L. All authors have read and agreed to the published version of the manuscript.

Funding: This work was supported by Korea Agency for Infrastructure Technology Advancement (KAIA) through the Ministry of Land, Infrastructure and Transport under Grant RS-2024-00417481.

Data Availability Statement: The original contributions presented in this study are included in this article. Further inquiries can be directed to the corresponding author.

Conflicts of Interest: The authors declare no conflicts of interest.

References

1. Yang, X.; Li, X.; Ning, B.; Tang, T. A Survey on Energy-Efficient Train Operation for Urban Rail Transit. *IEEE Trans. Intell. Transp. Syst.* **2016**, *17*, 2–13. [CrossRef]
2. Zhao, X.-H.; Ke, B.-R.; Lian, K.-L. Optimization of Train Speed Curve for Energy Saving Using Efficient and Accurate Electric Traction Models on the Mass Rapid Transit System. *IEEE Trans. Transport. Electrif.* **2018**, *4*, 922–935. [CrossRef]
3. Lee, J.-S.; Choi, U.-M. Velocity Profile based Evaluation and Improvement of Lifetime of Power Devices in Railway Propulsion Inverters. *IEEE J. Emerg. Sel. Top. Power Electron.* **2022**, *10*, 1384–1394. [CrossRef]
4. Gubarevych, O.; Duer, S.; Melkonova, I.; Woźniak, M.; Paś, J.; Stawowy, M.; Rokosz, K.; Zajkowski, K.; Bernatowicz, D. Research on and Assessment of the Reliability of Railway Transport Systems with Induction Motors. *Energies* **2023**, *16*, 6888. [CrossRef]
5. Zhao, X.; Phukan, R.; Chang, C.-W.; Burgos, R.; Uicich, S.; Asfaus, P.; Debbou, M.; Plat, A.; Dong, D. Design and Implementation of SiC-Based 200-kW High-Density High-Speed High-Altitude Electric Propulsion AC Drive System. *IEEE J. Emerg. Sel. Top. Power Electron.* **2024**, *12*, 5176–5199. [CrossRef]
6. Tripathi, A.; Narayanan, G. Torque Ripple Minimization in Neutral-Point-Clamped Three-Level Inverter Fed Induction Motor Drives Operated at Low-Switching-Frequency. *IEEE Trans. Ind. Appl.* **2018**, *54*, 2370–2380. [CrossRef]
7. Chen, F.; Qiao, W.; Wang, H.; Qu, L. A Simple Zero-Sequence Voltage Injection Method for Carrier-Based Pulsewidth Modulation of the Three-Level NPC Inverter. *IEEE J. Emerg. Sel. Top. Power Electron.* **2021**, *9*, 4687–4699. [CrossRef]
8. Gu, M.; Wang, Z.; Dordevic, O. Analysis and Reduction of Current and Voltage Ripple in DC Link for Three-Level NPC Inverter-Fed Dual Three-Phase Motor Drives. *IEEE Trans. Power Electron.* **2023**, *38*, 5128–5140. [CrossRef]
9. Lai, R.; Wang, F.; Burgos, R.; Boroyevich, D.; Jiang, D.; Zhang, D. Average Modeling and Control Design for VIENNA-Type Rectifiers Considering the DC-Link Voltage Balance. *IEEE Trans. Power Electron.* **2009**, *24*, 2509–2522.
10. Jiao, Y.; Lee, F.C.; Lu, S. Space Vector Modulation for Three-Level NPC Converter With Neutral Point Voltage Balance and Switching Loss Reduction. *IEEE Trans. Power Electron.* **2014**, *29*, 5579–5591. [CrossRef]
11. Alsofyani, I.M.; Lee, K.B. Three-level Inverter-fed Model Predictive Torque Control of a Permanent Magnet Synchronous Motor with Discrete Space Vector Modulation and Simplified Neutral Point Voltage Balancing. *J. Power Electron.* **2022**, *22*, 22–30. [CrossRef]
12. Lee, H.-J.; Kim, S.; Yoon, Y.-D. Accurate Neutral Current Control for Neutral Point Voltage Balancing in Three-Level Inverters Considering Digital Control and PWM Delay. In Proceedings of the 2019 IEEE Energy Conversion Congress and Exposition (ECCE), Baltimore, MD, USA, 29 September–3 October 2019.
13. Lee, H.-J.; Woo, T.-g.; Kim, S.; Yoon, Y.-D. Improved Neutral-Point Voltage Balancing Control With Time Delay Compensation and Antiwindup Loop for a Three-Level NPC Inverter. *IEEE Trans. Ind. Appl.* **2021**, *57*, 4970–4980. [CrossRef]
14. Zorig, A.; Barkat, S.; Sangwongwanich, A. Neutral point voltage balancing control based on adjusting application times of redundant vectors for three-level NPC inverter. *IEEE J. Emerg. Sel. Top. Power Electron.* **2022**, *10*, 5604–5613. [CrossRef]

15. Go, Y.-M.; Lee, J.-S. Offset Voltage Injection Method to Suppress the AC Voltage Ripple at a Neutral-Point in a Vienna Rectifier. *J. Power Electron.* **2023**, *23*, 1400–1410. [CrossRef]
16. Jiao, Y.; Lee, F.C. New Modulation Scheme for Three-Level Active Neutral-Point-Clamped Converter With Loss and Stress Reduction. *IEEE Trans. Ind. Electron.* **2015**, *62*, 5468–5479. [CrossRef]
17. Guan, Q.-X.; Li, C.; Zhang, Y.; Wang, S.; Xu, D.; Li, W.; Ma, H. An Extremely High Efficient Three-Level Active Neutral-Point-Clamped Converter Comprising SiC and Si Hybrid Power Stages. *IEEE Trans. Power Electron.* **2018**, *33*, 8341–8352. [CrossRef]
18. Song, W.; He, W.; Zhang, Z.; Ma, C.; Li, J. Active Thermal Control and Power Loss Reduction Scheme for Three-Level Active Neutral-Point-Clamped Inverters With Hybrid Modulation. *IEEE J. Emerg. Sel. Top. Power Electron.* **2024**, *12*, 1629–1640. [CrossRef]
19. Song, M.-G.; Kim, S.-M.; Lee, K.-B. Elimination of Abnormal Output Voltage in a Hybrid Active NPC Inverter. *IEEE Trans. Power Electron.* **2021**, *36*, 5348–5361. [CrossRef]
20. Lee, J.-Y.; Lee, J.-S. A normalized compensation method for voltage nonlinearity of three-level ANPC inverter. *J. Power Electron.* **2024**, *24*, 1286–1296. [CrossRef]
21. Chen, D.; Kong, W.; Qu, R.; Zhou, L. Correction of Field Orientation Inaccuracy Caused by Resolver Periodic Error and Rotor Time Constant Variation for Indirect Field-Oriented Control Induction Motor Drives. *IEEE Trans. Ind. Electron.* **2022**, *69*, 4440–4450. [CrossRef]
22. Elgbaily, M.; Anayi, F.; Alshbib, M.M. A Combined Control Scheme of Direct Torque Control and Field-Oriented Control Algorithms for Three-Phase Induction Motor: Experimental Validation. *Mathematics* **2022**, *10*, 3842. [CrossRef]
23. Holmes, D.G.; McGrath, B.P.; Parker, S.G. Current Regulation Strategies for Vector-Controlled Induction Motor Drives. *IEEE Trans. Ind. Electron.* **2012**, *59*, 3680–3689. [CrossRef]
24. Sengamalai, U.; Anbazhagan, G.; Thentral, T.M.T.; Vishnuram, P.; Khurshaid, T.; Kamel, S. Three Phase Induction Motor Drive: A Systematic Review on Dynamic Modeling, Parameter Estimation, and Control Schemes. *Energies* **2022**, *15*, 8260. [CrossRef]
25. KousalyaV, V.; Singh, B. Optimized Reference Points Based Vector Control of Induction Motor Drive for Electric Vehicle. *IEEE Trans. Ind. Appl.* **2023**, *59*, 4164–4174. [CrossRef]
26. Kim, S.-U.; Choi, J.-H.; Kim, Y.-S. Vector Control of Induction Motors using Optimal Efficiency Control. *J. Power Electron.* **2002**, *2*, 67–75.
27. Shin, M.-H.; Hyun, D.-S.; Cho, S.-B. Maximum torque control of stator-flux-oriented induction machine drive in the field-weakening region. *IEEE Trans. Ind. Appl.* **2002**, *38*, 117–122. [CrossRef]
28. Wu, X.; Huang, W.; Lin, X.; Jiang, W.; Zhao, Y.; Zhu, S. Direct Torque Control for Induction Motors Based on Minimum Voltage Vector Error. *IEEE Trans. Ind. Electron.* **2021**, *68*, 3794–3804. [CrossRef]
29. Dong, Z.; Yu, Y.; Li, W.; Wang, B.; Xu, D. Flux-Weakening Control for Induction Motor in Voltage Extension Region: Torque Analysis and Dynamic Performance Improvement. *IEEE Trans. Ind. Electron.* **2017**, *65*, 3740–3751. [CrossRef]
30. Buticchi, G.; Gerada, D.; Alberti, L.; Galea, M.; Wheeler, P.; Bozhko, S.; Peresada, S.; Zhang, H.; Zhang, C.; Gerada, C. Challenges of the Optimization of a High-Speed Induction Machine for Naval Applications. *Energies* **2019**, *12*, 2431. [CrossRef]
31. Klerk, M.L.D.; Saha, A.K. A Comprehensive Review of Advanced Traction Motor Control Techniques Suitable for Electric Vehicle Applications. *IEEE Access* **2021**, *9*, 125080–125108. [CrossRef]
32. Kim, J.-S.; Kim, D.-H.; Lee, J.-H.; Lee, J.-S. Smooth Pulse Number Transition Strategy Considering Time Delay in Synchronized SVPWM. *IEEE Trans. Power Electron.* **2023**, *38*, 2252–2261. [CrossRef]
33. Bae, B.-H.; Sul, S.-K. A compensation method for time delay of full-digital synchronous frame current regulator of PWM AC drives. *IEEE Trans. Ind. Appl.* **2003**, *39*, 802–810. [CrossRef]
34. Abouzeid, A.F.; Guerrero, J.M.; Endemano, A.; Muniategui, I.; Ortega, D.; Larrazabal, I.; Briz, F. Control Strategies for Induction Motors in Railway Traction Applications. *Energies* **2020**, *13*, 700. [CrossRef]
35. Fang, X.; Lin, S.; Yang, Z.; Lin, F.; Sun, H.; Hu, L. Adhesion Control Strategy Based on the Wheel-Rail Adhesion State Observation for High-Speed Trains. *Electronics* **2018**, *7*, 70. [CrossRef]
36. Song, X.; Wang, W.; Zhang, S.; Guo, J.; Zhao, X.; Qi, H.; Ding, H.; Zhou, Z. Effects of torque adjustment rates and increments on wheel-rail adhesion instability behavior under various speed and axle load conditions. *Wear* **2025**, 572–573, 206026. [CrossRef]

Disclaimer/Publisher's Note: The statements, opinions and data contained in all publications are solely those of the individual author(s) and contributor(s) and not of MDPI and/or the editor(s). MDPI and/or the editor(s) disclaim responsibility for any injury to people or property resulting from any ideas, methods, instructions or products referred to in the content.